JOURNAL OF CHEMICAL PHYSICS VOLUME 117, NUMBER 13 1 OCTOBER 2002

Shear viscosity of a supercooled polymer melt via nonequilibrium molecular dynamics simulations

F. Varnik[a)]
CECAM, ENS-Lyon, 46 Allée d'Italie, 69007 Lyon, France and Institut für Physik, Johannes Gutenberg-Universität, D-55099 Mainz, Germany

K. Binder
Institut für Physik, Johannes Gutenberg-Universität, D-55099 Mainz, Germany

(Received 21 May 2002; accepted 9 July 2002)

Using nonequilibrium molecular dynamics simulations, we compute the shear viscosity, η_s, of a glass forming polymer melt at temperatures ranging from the normal liquid state down to the supercooled state. For this purpose, the polymer melt is confined between two solid walls and a constant force pointing in direction parallel to the walls is applied on each monomer thus giving rise to a Poiseuille flow. It is shown that $\eta_s(T)$ does not exhibit an Arrhenius-type behavior but can be described both by a power law (mode coupling theory) and by a Vogel–Fulcher–Tammann law. A similar behavior is observed in recent experiments above the glass transition temperature. The diffusion coefficient is computed using the mean square displacements in direction perpendicular to the flow. Combined with the knowledge of $\eta_s(T)$, it is then shown that the Stokes–Einstein relation is valid at high temperatures, whereas deviations are observed in the supercooled regime in agreement with experiments. Moreover, the local viscosity, $\eta(z)$, is also computed and its reliability is discussed. Using the sharp rise of $\eta(z)$ close to the wall, we estimate z_{wall}, the effective position of the wall. It is found that z_{wall} moves towards the film center at lower T thus leading to a decrease of the (hydrodynamic) width of the system. Furthermore, we observe that the curves for $\eta(z)/\eta_s$ at various temperatures superimpose if the data are depicted versus $z-z_{\mathrm{wall}}(T)$. This suggests that the spatial and temperature dependence of the local viscosity separate if the effective position of the wall is chosen as a new reference plane. © *2002 American Institute of Physics.*
[DOI: 10.1063/1.1503770]

I. INTRODUCTION

The properties of glass forming materials and in particular the glass transition itself have been the subject of extensive experimental and theoretical investigations.[1–5] These studies were enriched by important contributions from computer simulations[6,7] which have the advantage of providing more detailed information on the microscopic level. However, while estimating single-particle quantities from simulated data is rather a simple task, computing collective transport coefficients may prove more difficult. Within an ordinary (equilibrium) molecular dynamics (MD) simulation, for example, the self-diffusion coefficient can be obtained by monitoring the mean square displacements of a tagged particle, whereas the computation of the shear viscosity requires the use of the corresponding Green–Kubo relation, i.e., the evaluation of the integral over time of the stress autocorrelation function (ACF). However, it is well-known that an evaluation of the time integrals of autocorrelation functions in finite systems leads to vanishing results unless the integration is limited to a maximal time, $t_{\max}$, usually taken as the first zero of the ACF.[8,9]

Nonequilibrium molecular dynamics (NEMD) simulations provide an alternative way for the computation of transport coefficients.[10–12] The basic idea of this method is to study the response of the system under a weak external force field. In the present work, we are going to apply this technique for a study of the shear viscosity of a nonentangled[13] polymer melt in a temperature interval ranging from the normal liquid state down to the supercooled region. For this purpose, the system is confined between two solid walls and a constant force F^e is applied on each fluid atom (monomer). The situation is similar to that of a confined fluid subject to a uniform gravitational force acting in a direction parallel to the system boundaries. Sokhan, Nicholson, and Quirke, for example, used this approach to induce a Poiseuille flow in a simple fluid confined between two planar solid walls made of carbon atoms.[14] They studied the influence of both the surface corrugation and the adsorption potential on the hydrodynamic boundary condition with the result that even in the case of a strongly adsorbing potential a large slip length can be observed provided that the surface corrugation is not too high.

Rheological properties of the present polymer model (see Sec. II) have been studied in Ref. 15 via NEMD in order to obtain more evidence for a dynamical crossover which has already been observed in equilibrium studies of polymer melts.[16,17] During these rheological studies, the viscosity was determined for various chain lengths N_p as a function of the shear rate thus allowing an estimate of the chain length de-

---

[a)]Electronic mail: varnik@cecam.fr

Downloaded 27 Sep 2002 to 193.49.39.50. Redistribution subject to AIP license or copyright, see http://ojps.aip.org/jcpo/jcpcr.jsp

pendence of the viscosity in the limit of vanishing shear rate. As a result, a crossover from a Rouse-type behavior[18] ($\mathcal{D} \propto 1/N_p$, $\mathcal{D}$ being the self-diffusion constant of the chains) to the reptation regime[19] ($\mathcal{D} \propto 1/N_p^2$) was found at a chain length of $N_p = 100 \pm 10$. However, to our knowledge, a nonequilibrium simulation study of the *temperature dependence* of the viscosity and the Stokes–Einstein relation for a model of polymer melt near the glass transition has not been done yet. This is one of the main objectives of the present work.

In real experiments a pressure gradient, ∇p, is often used to induce a flow. However, there is an alternative to this choice which is more suitable for molecular dynamics simulations. Consider a fluid subject to a homogeneous field exerting the force $F^e = F^e e_x$ on each individual particle. The momentum conservation equation for this system is[11,20,21]

$$\rho(\boldsymbol{r},t)\frac{\mathrm{d}u(\boldsymbol{r},t)}{\mathrm{d}t} = -\nabla\cdot\mathbf{P} + \rho(\boldsymbol{r},t)\boldsymbol{F}^e$$

$$= -\nabla\cdot\Pi - \nabla p + \rho(\boldsymbol{r},t)\boldsymbol{F}^e, \tag{1}$$

where we introduced the *viscous pressure tensor* $\Pi = \mathbf{P} - p\mathbf{I}_{3\times 3}$ (p is the well-known hydrostatic pressure). Setting $\boldsymbol{F}^e = 0$ along with $\nabla p \neq 0$ in Eq. (1) corresponds to the case where the system is driven by a pressure gradient. On the other hand, the choice $\boldsymbol{F}^e \neq 0$ along with $\nabla p = 0$ is the situation we are going to study. The point is that the system cannot distinguish between these cases. In addition to the simplicity of implementation in a MD-code, the use of an external field instead of a pressure gradient allows the system to remain longitudinally homogeneous.[20] (In real experiments, the fluid remains nearly incompressible under the applied pressure gradient. However, to obtain a satisfactory signal to noise ratio, pressure gradients used in MD simulations are considerably higher and might lead to significant density variations. A combination of these density variations with periodic boundary condition would then lead to discontinuities in the density at system boundaries, i.e., when going from the basic simulation box to one of its adjacent image systems.)

We stress that the main objective of the present work is *not* a thorough study of the hydrodynamic boundary conditions and their dependence on the fluid–wall interactions, but an analysis of the temperature dependence of the shear viscosity at low temperatures. Nevertheless, we will give a short overview of what happens at system boundaries for two different choices of the wall–monomer interaction parameters. It will be shown that stronger attraction and a better adaptation of the fluid structure to the (periodic) structure of the wall lead to the so called stick boundary condition, whereas considering an interaction potential where wall and fluid atoms are equivalent gives rise to a large slip at the fluid–wall interface. In this respect, the results of our polymer model qualitatively agree with those obtained for simple liquids[9,22–24] and for thin films of hexadecane.[25]

The next section is devoted to an introduction of the model. In Sec. III we discuss the influence of the fluid–wall interaction parameters on the boundary condition. Section IV deals with different methods for removing the viscous heat in order to keep the system temperature constant. In particular, it is shown that temperature profiles are formed if the viscous heat is removed only through the heat transfer to the walls. The observed temperature profiles are found to be in good agreement with theoretical predictions.[26] The results of extensive MD simulations on the temperature dependence of the shear viscosity are presented in Sec. V. An analysis of the local viscosity, $\eta(z)$, is the subject of Sec. VI and Sec. VII presents our conclusions.

II. A BEAD–SPRING POLYMER MODEL AND THE WALLS

We study a bead–spring model of a monodisperse polymer melt[17,27] of short chains (each consisting of 10 monomers) embedded between two solid walls. Two potentials are used for the interaction between particles. The first one is a truncated and shifted Lennard-Jones (LJ) potential which acts between all pairs of particles,

$$U_{\mathrm{LJ}}(r) = \begin{cases} V_{\mathrm{LJ}}(r) - V_{\mathrm{LJ}}(r_{\mathrm{c}}) & \text{if } r < r_{\mathrm{c}}, \\ 0 \quad \text{otherwise}, \end{cases} \tag{2}$$

where $V_{\mathrm{LJ}}(r) = 4\epsilon_{ij}[(\sigma_{ij}/r)^{12} - (\sigma_{ij}/r)^6]$ and $r_{\mathrm{c}} = 2 \times 2^{1/6}\sigma_{ij}$. The index pair ij allows us to distinguish between monomer–monomer (mm), wall–monomer (wm), and wall–wall (ww) interactions. To ensure the connectivity between adjacent monomers of a chain, we use a FENE-potential,[17]

$$U_{\mathrm{FENE}}(r) = -\frac{k}{2}R_0^2 \ln\left[1 - \left(\frac{r}{R_0}\right)^2\right]. \tag{3}$$

Here, $k = 30\epsilon_{\mathrm{mm}}/\sigma_{\mathrm{mm}}^2$ is the strength factor and $R_0 = 1.5\sigma_{\mathrm{mm}}$ the maximum allowed length of a bond. If not explicitely mentioned, all lengths are measured in units of a monomer diameter σ_{mm}, all masses in units of monomer mass m_{mm} and energy in units of ϵ_{mm}. Other quantities are measured in suitable combinations of these basic units. The unit of temperature, for example, is $\epsilon_{\mathrm{mm}}/k_{\mathrm{B}}$, ($k_{\mathrm{B}} = 1$), that of time $\sigma_{\mathrm{mm}}\sqrt{m_{\mathrm{mm}}/\epsilon_{\mathrm{mm}}}$, etc.

The left panel of Fig. 1 compares the bond potential (i.e., the sum of LJ- and FENE-potentials) with the LJ-potential. It shows that the bonded monomers prefer shorter distances than the nonbonded ones. Thus, our model contains two intrinsic length scales (see right panel of Fig. 1 for a schematic illustration). Since these length scales are chosen to be incompatible with a (fcc or bcc) crystalline structure and since our chains are flexible (no bond angle or torsion potentials), one could expect that the system does not crystallize at low temperatures, but remains amorphous.[28] Extensive equilibrium studies of the present model showed that the model is indeed suitable for the study of the glass transition both in the bulk and in confined geometry.[27,29–32]

In the present simulation, the system is confined between two layers of triangular lattice sites, $r_{i,\mathrm{eq}}$. A wall atom is coupled to its lattice site by a harmonic potential,

$$U_{\mathrm{harm}}(r_i) = \tfrac{1}{2}K_{\mathrm{harm}}|\boldsymbol{r}_i - \boldsymbol{r}_{i,\mathrm{eq}}|^2. \tag{4}$$

The force constant, K_{harm}, is a measure of the stiffness of the harmonic spring. We set $K_{\mathrm{harm}} = 100$ which is close to 114.3, the force constant corresponding to the harmonic approximation of the LJ-force in a fcc-lattice. This choice is motivated

Downloaded 27 Sep 2002 to 193.49.39.50. Redistribution subject to AIP license or copyright, see http://ojps.aip.org/jcpo/jcpcr.jsp

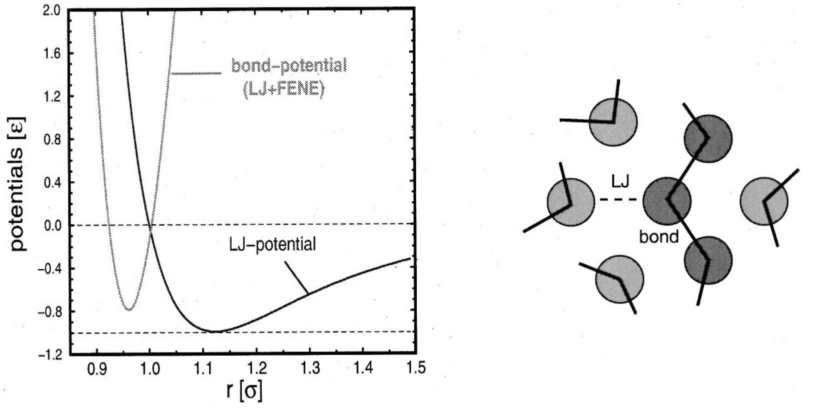

FIG. 1. Left panel: Lennard-Jones potential (LJ) vs the bond potential, the sum of the LJ and FENE potentials. The bond potential is shifted by 20ϵ to lower values for the sake of comparison with the LJ potential. The minimum position of the bond-potential is smaller than that of the LJ-potential: The bond potential has its minimum at $r \cong 0.96\sigma$, whereas that of a pure LJ-potential lies at $r = \sqrt[6]{2}\sigma$. Due to the incompatibility of these length scales and due to the flexibility of our model (no bond angle or torsion potentials), one expects that cooling the system would not lead to crystallization, but the system maintains the amorphous structure typical of the liquid phase.

by comparable simulation on simple liquids.[20] Each wall atom interacts with monomers via a Lennard-Jones potential [see Eq. (2)] with σ_{wm} the preferred monomer–wall distance and ϵ_{wm} the depth of the corresponding potential well.

We emphasize here that our goal is not a realistic description of monomer–wall interactions for polymer melts; rather we wish to study a generic model, suitable as a tool to calculate shear viscosity over a wide temperature range. Therefore, in order to make sure that polymers would not penetrate the walls, we have introduced an additional potential barrier acting on the monomers via

$$U_{\mathrm{w}}(d) = \epsilon_{\mathrm{mm}} \left(\frac{\sigma_{\mathrm{mm}}}{d} \right)^{9}. \tag{5}$$

Here, $d = |z_{\text{particle}} - z_{\text{smooth wall}}|$, where $z_{\text{smooth wall}} = \pm(\sigma_{\mathrm{mm}} + D/2)$. D denotes the separation between the solid walls, i.e., the distance between the triangular layers on the left and right side of the system. The potential $U_{\mathrm{w}}(d)$ qualitatively corresponds to an average potential arising from wall layers behind the first one in the case of an infinitely thick wall. The use of an additional wall potential in order to prevent a penetration of the atomistic walls is not new. It was, for example, used in Ref. 25 in MD studies of the wall slip in thin films of hexadecane.

A snapshot of the simulation box is shown in Fig. 2 at a temperature of $T = 0.44$ [$L_x = L_y = 10.05$, $D = 21$. Periodic boundary conditions are applied in x and y directions only. In the x direction, a constant shear force, F^e, is applied on each monomer.

Two lateral system sizes have been investigated during our simulations: $L_x = L_y = 11.11$ and $L_x = L_y = 10.05$. In both cases, the number of particles is $N = 2000$ and the distance between the solid walls is $D = 20$. The reason for a change of the lateral system size was the observation of a phase separation (partial drying at the wall) at low temperature for $L_x = L_y = 11.11$. This phenomenon is avoided at all T for the smaller lateral dimension.

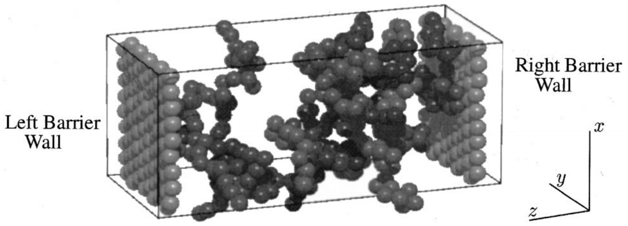

FIG. 2. A snapshot of the simulation box at $T = 0.44$. Each wall is modeled as a layer of atoms arranged on a triangular lattice and an additional potential [see Eq. (5)] indicated by solid lines on the left and on the right side of the system. The lateral system size is $L_x = L_y = 10.05$. The system is periodically repeated in x and y directions. The distance between triangular lattice planes is chosen to $D = 20$. On each monomer a constant shear force acts pointing in the x direction: $\boldsymbol{F}^e = F^e \boldsymbol{e}_x$. To visualize the chain structure, a continuous gray scaling is used for different chains. Note also that only 40 chains (from the total of 200 chains, containing 2000 monomers) are shown here.

III. CHOICE OF THE INTERACTION PARAMETERS

Choosing $\sigma_{ij} = 1$ and $\epsilon_{ij} = 1$ for all interactions (i.e., monomer–monomer, monomer–wall, and wall–wall), we first performed simulations at $T = 1$ ($L_x = L_y = 11.11$, $F^e = 0.03$). The velocity profile $u_x(z)$ is then obtained as a statistical average of one particle velocities,

$$u_x(z) = \left\langle \sum_{i=1}^{N} v_{x,i}\, \delta(z_i - z) \right\rangle \Big/ (A\rho(z)). \tag{6}$$

Here, $\langle \cdots \rangle$ denotes thermal averaging, N is the total number of monomers ($N = 2000$ for all simulations reported here) and $A = L_x L_y$ the surface area of the wall.

As demonstrated in Fig. 3, the above choice of interaction parameters leads to a large jump in the velocity profile very close to the walls thus indicating that, on a microscopic level, the velocity profile at the solid–liquid interface can be different from the classical "nonslip" (or stick) assumptions of hydrodynamics. The occurence of such a "partial slip" effect has also been observed both in experiments[33–35] and in molecular dynamics studies of soft spheres,[9] of binary mixtures[22,23,36] and of polymers.[25,37–40]

The partial slip effect can be quantified by introducing *two* parameters, namely, the position z_{wall}, where the slippage is to be measured, and the slip length δ,[9]

$$\left. \frac{\partial u_x(z)}{\partial z} \right|_{z = z_{\mathrm{wall}}} = \frac{u(z_{\mathrm{wall}})}{\delta}. \tag{7}$$

Thus, the slip length gives the distance between z_{wall} and the intersection point with the z-axis of the tangent line on $u_x(z)$ at $z = z_{\mathrm{wall}}$ (see Fig. 3).

Downloaded 27 Sep 2002 to 193.49.39.50. Redistribution subject to AIP license or copyright, see http://ojps.aip.org/jcpo/jcpcr.jsp

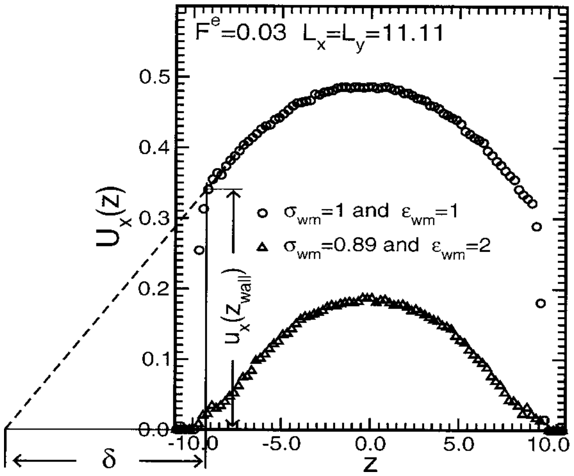

FIG. 3. Velocity profile as obtained from MD-simulations at a temperature of $T=1$, $F^e=0.03$, and $L_x=L_y=11.11$. Two choices of the parameters of wall–monomer interactions are compared. A partial slip is observed for the case where the wall atoms (w) have the same size and the same interaction energy as the inner monomers (m). The dashed line extrapolates the velocity profile at the wall ($z=z_{\mathrm{wall}}$) towards the z-axis and illustrates an estimation of the slip length δ [see Eq. (7), note that z_{wall} is not identical to the plane of the solid walls ($z=\pm 10$) but has a distance of approximately one monomer diameter with the latter]. Increasing the interaction energy and reducing the preferred wall-monomer distance leads to a stick boundary condition.

Now, for a Poiseuille flow satisfying the hydrodynamic boundary condition given in Eq. (7), the velocity profile reads[9]

$$u_x(z)=\frac{-\rho_0 F^e}{2\eta_s}(z^2-z_{\mathrm{wall}}^2-2z_{\mathrm{wall}}\delta), \tag{8}$$

where $\rho_0=\rho(z=0)$ is the density in the middle of the film, F^e is the driving force per particle, η_s stands for the shear viscosity, and D is the wall-to-wall separation. In deriving Eq. (8), it is assumed that the flow is confined between two identical walls, that the film center lies at $z=0$ and that $z_{\mathrm{wall}}>0$ denotes the absolute distance of the walls from the film center (i.e., the walls are placed at $\pm z_{\mathrm{wall}}$). Note that, as F^e and ρ_0 are well known, the knowledge of the prefactor of the quadratic term is sufficient to uniquely determine the shear viscosity.

To improve the stick boundary condition, we favor the wall-monomer interaction compared to that between particles of the same type. This was achieved by setting $\sigma_{\mathrm{wm}}=2^{-1/6}\approx 0.89$ and $\epsilon_{\mathrm{wm}}=2$. Figure 3 shows that this choice does indeed lead to a stick boundary condition. Qualitatively, this can be understood as follows: The wall–monomer interaction is favored in two ways. First, as $\sigma_{\mathrm{wm}}<\sigma_{\mathrm{ww}}=\sigma_{\mathrm{mm}}$, a monomer can come closer to a wall atom than to another monomer inside the system. Second, the energy cost to separate a wall atom from an inner atom (monomer) is twice as large as the price one must pay to separate two particles of the same type. This makes plausible why the monomers "stick" much better to the solid walls compared to the case where all interaction parameters were set to unity.

Figure 4 depicts the density profiles at $T=1$, $F^e=0.03$, and $L_x=L_y=11.11$ for the two choices of the parameters of the wall–monomer interaction. As seen from this figure, an enhancement of the density peaks close to the solid wall is observed for the choice of a stronger wall–monomer attraction ($\epsilon_{\mathrm{wm}}=2$ and $\sigma_{\mathrm{wm}}\approx 0.89$). In other words, the system better "wets" the wall. The slightly different densities at the film center are due to the fact that the particle number and the system volume are kept constant. A change of the density close to the walls thus reflects itself in an opposite change of the density at the film center.

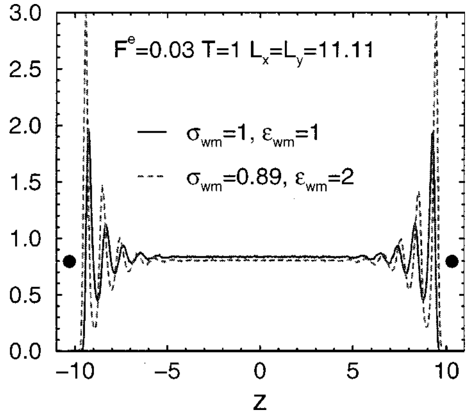

FIG. 4. Density profiles at $T=1$, $F^e=0.03$, and $L_x=L_y=11.11$ for two choices of the parameters of wall–monomer interaction: Compared to $\sigma_{\mathrm{wm}}=1$ and $\epsilon_{\mathrm{wm}}=1$ [which corresponds to the partial slip case, see Fig. 3], the density close to the walls is more pronounced for the choice of $\sigma_{\mathrm{wm}}=0.89$ and $\epsilon_{\mathrm{wm}}=2$. As the volume and the particle number are constant, this leads to a slightly lower density in the inner part of the film. The filled black circles indicate the position of the solid walls.

A better understanding of how the particles "stick" to the solid walls is obtained by looking at the pair distribution function measured in a plane parallel to the wall,

$$g(z,r)=\frac{1}{A\rho^2(z)}\left\langle \sum_{j\neq i} \delta(\boldsymbol{r}-\boldsymbol{r}_{ij})\,\delta(z-z_i)\,\delta(z-z_j)\right\rangle. \tag{9}$$

Here, z is the distance of the plane from the wall, A the surface area of the wall and $\rho(z)$ the monomer density at z. The prefactor $1/A\rho^2(z)$ ensures that $\lim_{r\to\infty} g(z,r)=1$.

The upper panel of Fig. 5 depicts $g(z,r)$ for a plane at the contact with the wall for both choices of the interaction parameters. As seen from this panel, in the case of a strong monomer–wall attraction ($\epsilon_{\mathrm{wm}}=2$ and $\sigma_{\mathrm{wm}}\approx 0.89$, leading to a stick boundary condition) the packing structure of the system in the very vicinity of the wall is strongly effected by the periodic arrangement of the wall atoms. This favors a more efficient "sticking" of the fluid atoms to the wall. For the case of $\epsilon_{\mathrm{wm}}=1$ and $\sigma_{\mathrm{wm}}=1$ (corresponding to the partial slip situation), this effect is much weaker.

Apart from the mentioned qualitative arguments, the observed decrease of the slip length in the case of the strong monomer–wall interaction can also be understood within a theoretical approach. Using the linear response theory, it was shown in Ref. 23 that the slip length scales as

$$\delta \propto \frac{1}{S_{\mathrm{c}}(q)\,\epsilon_{\mathrm{wm}}^2\rho_{\mathrm{c}}}. \tag{10}$$

Downloaded 27 Sep 2002 to 193.49.39.50. Redistribution subject to AIP license or copyright, see http://ojps.aip.org/jcpo/jcpcr.jsp

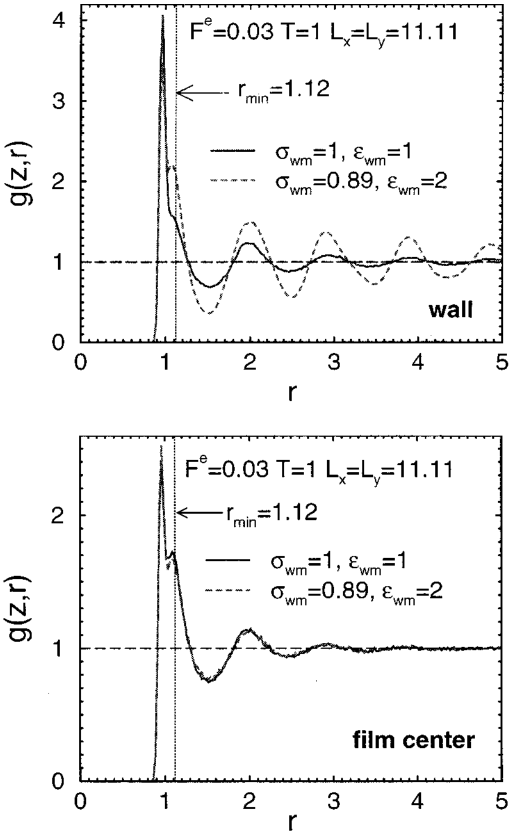

FIG. 5. Upper panel: The radial pair distribution function, $g(z,r)$, computed within the first density layer in the vicinity of the solid wall. For $\sigma_{\mathrm{wm}}=1$ and $\epsilon_{\mathrm{wm}}=1$ (solid line) the periodic structure of the wall does not change much the packing structure of the system in the (x,y) plane. The situation is strongly different in the case of $\sigma_{\mathrm{wm}}=0.89$ and $\epsilon_{\mathrm{wm}}=2$ (dashed line). The arrangement of monomers parallel to the wall is mainly induced by the lattice structure of the wall. The vertical dotted line indicates the minimum position of the Lennard-Jones potential [the first peak of $g(z,r)$ does not occur at this distance, but at a smaller one corresponding to the minimum position of the bond potential $r_{\mathrm{bond}}\approx 0.96$]. Lower panel: Same as in the upper panel, now for a layer in the film center. Obviously, far from the wall, the structure of the melt is amorphous for both choices of interaction parameters.

Here, ρ_{c} is the density in the layer at contact with the wall and $S_{\mathrm{c}}(q)$ is the structure factor measured in the (x,y)-plane within the same layer for $q=\sqrt{q_x^2+q_y^2}=2\pi/\sigma_{\mathrm{mm}}$ [$\approx$peak position of $S_{\mathrm{c}}(q)$].

Equation (10) shows that the slip length is proportional to the inverse of the square of ϵ_{wm}. Note also that ρ_{c} increases with a growing ϵ_{wm} (see Fig. 4). Furthermore it is clear from the upper panel of Fig. 5 that also $S_{\mathrm{c}}(q)$ [i.e., the Fourier transform of $g(z=z_{\mathrm{wall}},r)$] will exhibit a larger peak value for the wetting case. The variation of ρ_{c} and $S(q)$ thus amplifies the effect of an increase in ϵ_{wm} and enforces the decrease of the slip length.

On the other hand, it is seen from the lower panel of Fig. 5 that, in the film center, the system exhibits an amorphous structure regardless of the monomer–wall interaction. This is an important point for the study of bulklike properties of the model within the present nonequilibrium simulations. The restriction of the data analysis to a region around the film center would then allow a determination of the transport coefficients with negligible wall effects.

The simulation results we are going to discuss below all correspond to the "stick" boundary condition, i.e., to the choice of $\sigma_{\mathrm{wm}}=0.89$ and $\epsilon_{\mathrm{wm}}=2$ (in units of σ_{mm} and ϵ_{mm}). The parameters of the interaction among wall atoms, on the other hand, remain unchanged: $\sigma_{\mathrm{ww}}=1$ and $\epsilon_{\mathrm{ww}}=1$.

IV. ON THERMOSTATING METHODS

The external force F^e does work on the system. Therefore, in order to keep the system temperature at a predefined value, the extra heat must be removed by some thermostating mechanism. A way to achieve this objective is to keep the walls at a constant temperature by coupling them to a heat bath. A steady state is then reached when the rate of energy transfer from the inner part of the system to the walls equals that created by the external force. An advantage of this method is that the fluid dynamics is purely Newtonian and thus is not perturbed by a coupling of the particle velocities to a heat bath. The drawback of the method is, however, that the heat transfer towards the walls is driven by a temperature gradient. As a consequence, a temperature profile is formed across the film.

It is easy to see that the energy creation rate in a thin layer of thickness dz placed at z is given by $AF^e u_x(z)\rho(z)\mathrm{d}z$, where A is the surface area of the wall (note that the number of particles in $[z\, z+\mathrm{d}z]$ is $A\rho(z)\mathrm{d}z$). Using this relation along with the energy transport and the momentum conservation equations of hydrodynamics,[41] the resulting temperature profile for the present situation is given by (see for instance, Ref. 26)

$$T(z)=T_{\mathrm{wall}}+\frac{\rho^2 F^{e2} D^4}{192\lambda\,\eta_s}\left[1-\left(\frac{z}{D/2}\right)^4\right]. \tag{11}$$

Here, T_{wall} is the temperature of the (thermostated) wall, ρ is the (average) system density, λ is the heat conductivity, η_s is the viscosity of the fluid, and D is the distance between solid walls. As expected, the temperature is maximal at the film center ($z=0$) and minimal at the wall ($z=D/2$).

We performed simulations at a temperature of $T=1$ while varying F^e. For each value of F^e, the number of independent runs was 10 and the duration of each run was 10^6 MD steps. The system size was $L_x=L_y=11.11$ [leading to a density of $\rho(z=0)=0.795$ at the film center]. Note that, in deriving Eq. (11), it is assumed that λ, ρ, and η_s are spatially constant. Despite this approximation, Fig. 6 shows that the temperature profiles obtained from the simulation can very well be described by Eq. (11).

Figure 7 depicts the velocity profiles measured during the same set of simulations. As seen from this figure, deviations from a quadratic z-dependence are enhanced for larger values of the shear force. However, even for the largest value of F^e shown in this figure, the velocity profile around the film center ($z\in[-5\ 5]$) is well fitted by Eq. (8). As a result of these fits, we obtain η_s for various values of the shear force.

Results for η_s are depicted in Fig. 8. First, as expected, at small F^e, η_s is practically independent of the driving force. It is seen from Fig. 8 that $5.5\lesssim\lim_{F^e\to 0}\eta_s\lesssim 6$. For the same model and at the same temperature ($T=1$) we read

Downloaded 27 Sep 2002 to 193.49.39.50. Redistribution subject to AIP license or copyright, see http://ojps.aip.org/jcpo/jcpcr.jsp

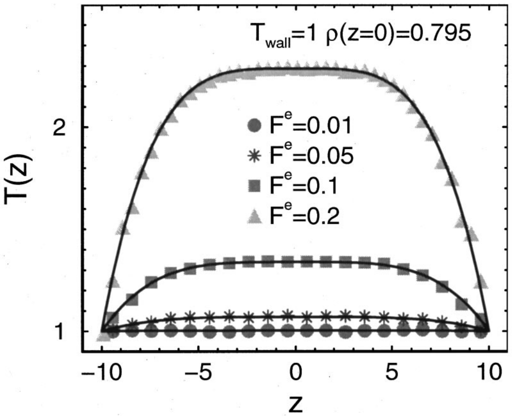

FIG. 6. A comparison of the temperature profiles resulting from MD simulations (symbols) with the theoretical prediction Eq. (11) (lines) for various values of F^e. The fluid particles were not coupled with a heat bath but obeyed pure Newtonian dynamics. The only mechanism to regulate the system temperature was the energy transfer towards the (thermostated) walls. Note that, in computing the local temperature at z, we subtract the streaming velocity, $u(z)$, from the instantaneous velocities of all particles in interval $[z,z+\mathrm{d}z]$, i.e., we evaluate $T(z)=\langle[v_i-u(z)]^2\rangle$ for a tagged particle i inside the interval $[z,z+\mathrm{d}z]$.

from Fig. 1 in Ref. 15, $\eta_s\approx 7$ at zero shear rate limit. This result is quite reasonable as the density in Ref. 15 is slightly higher than in our case [$\rho=0.84$ compared to $\rho(z=0)=0.795$].

However, at larger values of F^e, significant change in η_s is observed. As to the average temperature, i.e., $T=\int_{-D/2}^{D/2}T(z)\mathrm{d}z/D$, a quadratic dependence on F^e is observed as expected from Eq. (11). Hence, the rapid decrease of the shear viscosity as a function of F^e is partly a consequence of increasing temperature.

Using the results on the viscosity (see Fig. 8) we obtain from fits to Eq. (11) an estimation of the heat conductivity in the melt: $3\lesssim\lambda\lesssim 4.4$ for all applied shear forces. As the average system temperature varies from $T\approx 1$ to $T\approx 2.3$ within the same F^e-range, our result on λ suggests that the heat conductivity does not depend much on temperature. The insensitivity of the heat conductivity with respect to a temperature change has also been reported from experiments on *o*-terphenyl mixtures.[42]

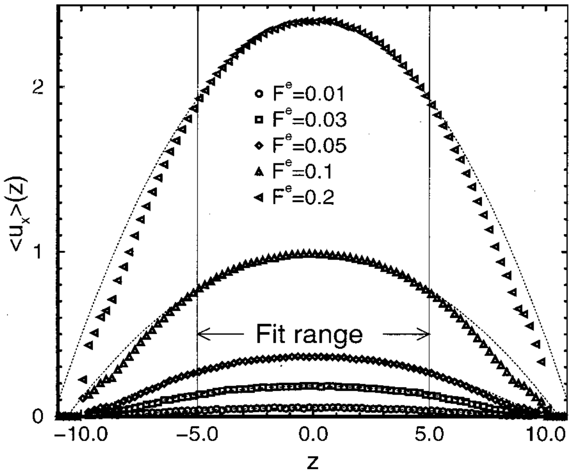

FIG. 7. Profiles of the streaming velocity, $u_x(z)$, for various values of the driving force and the corresponding fits to Eq. (8). As indicated in the figure, only values with $z\in[-5\ 5]$ are taken into account in the fit procedure. This reduces the effects of the walls and thus leads to a better estimate of the shear viscosity, η_s.

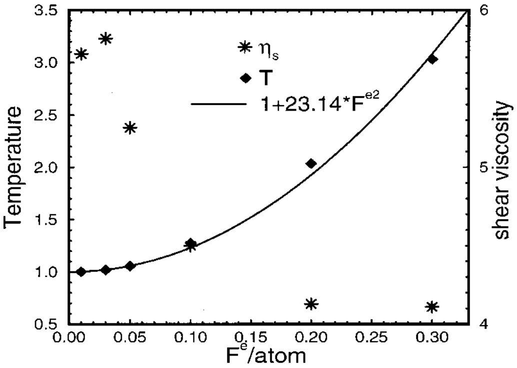

FIG. 8. Average system temperature versus the driving force per atom (diamonds). The solid line represents a best fit to $T-T_{\mathrm{wall}}\propto F^{e2}$ obtained by averaging Eq. (11) over the whole film ($T_{\mathrm{wall}}=1$). The asterisks show the shear viscosity obtained from fits to Eq. (8) of the streaming velocity profile (see also Fig. 7).

The huge temperature changes demonstrated in Fig. 6 may hide, to some extent, the variation of T at smaller F^e. Therefore, we note that a temperature change of 2% was observed at a relative small driving force of $F^e=0.03$. However, due to the dramatic change of the system dynamics with temperature in the supercooled state,[27,29,31] a temperature change of 2% in this regime is not tolerable. A way out of this situation would be the choice of a smaller shear force. But, as seen from Fig. 7, already at the very high temperature of $T=1$ the amplitude of the velocity profile is very weak for $F^e=0.01$. The choice of such a small F^e would therefore lead to extremely small signal to noise ratios in the velocity profile at low temperatures.

It is therefore desirable to have a safer control of the system temperature than provided by the energy exchange with the walls. The simplest way, of course, would be to apply the thermostating algorithm not only to the wall atoms, but also to the polymer chains. Recalling the definition of the temperature in a flow, $T\equiv m\langle(v-\langle v\rangle)^2\rangle/3k_{\mathrm{B}}$, we see that a direct thermostating of the inner part of the system requires the knowledge of the velocity profile $u_x(z)\equiv\langle v_x\rangle(z)$ (note that $\langle v_y\rangle=\langle v_z\rangle=0$).

This problem was solved in the following way: For each run, the velocity profile was calculated during the preceding equilibration period (with "equilibration," we mean the very first simulation stage, during which the system reaches a steady state). Note that, as the equilibration is a necessary part of a MD simulation, it does not require extra computation power. The equilibration itself starts with $u_x(z)\equiv 0$ and improves this initial "guess" by sampling velocities. That this procedure does indeed lead to a spatially constant temperature profile is demonstrated in Fig. 9. As shown in this figure, $T(z)$ is constant across the film to a high degree of accuracy.

The reader may have noticed that, contrary to the data presented so far, Fig. 9 shows results obtained at a higher

Downloaded 27 Sep 2002 to 193.49.39.50. Redistribution subject to AIP license or copyright, see http://ojps.aip.org/jcpo/jcpcr.jsp

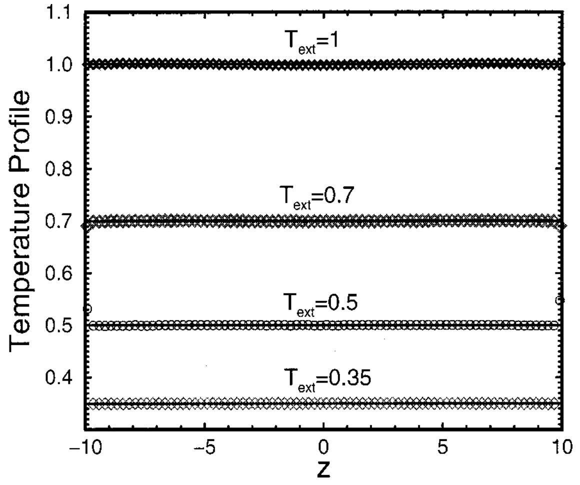

FIG. 9. Temperature profile at a shear force of $F^e=0.05$ for a system size of $L_x=L_y=10.05$ [leading to a density of $\rho(z=0)=0.99$ at the film center]. Note that the streaming velocity is subtracted from the particle velocities when computing the local temperature: $T(z)=m\langle v_i-\langle v_i\rangle(z)\rangle^2/3k_B$ for a tagged particle i with $z_i\in[z\ z+\mathrm{d}z]$ $(m=1,\ k_B=1)$. All profiles coincide with horizontal lines indicating the corresponding imposed temperature T_{ext}.

density in the film center of $\rho_0=0.99$ (which corresponds to the lateral system size of $L_x=L_y=10.05$) and not at $\rho_0=0.795$ $(L_x=L_y=11.11)$. In fact, all simulations whose results we are going to discuss in the next sections have been performed using the smaller system size. The reason for this choice is that for $T<0.9$ a sort of phase separation develops if $L_x=L_y=11.11$. In particular, the density profile is no longer symmetric but a region of low density occurs close to one of the walls.

This situation is depicted in Fig. 10 for $T=0.8$. This figure shows that out of 10 independent runs, in 4 cases a sort of "partial drying" occurs at the left wall and in the remaining 6 runs at the right wall. At low temperatures, the system tries to contract in order to increase the density. However, a volume change is not feasible in a NVT-ensemble simulation. The higher density in the film center is therefore achieved by particle transport from the walls towards the inner part. Obviously, such a transport does in general not set in simultaneously at both walls but first develops at one of the walls. Suppose that a particle current towards the film center first sets in at the left wall. As a consequence, the system density close to this wall decreases, while at the same time it increases in the remaining part of the film approaching the value consistent with the actual temperature. A phenomenon analogous to the present one is the formation of regions of extremely low density (holes) at low temperatures observed in constant volume MD-simulations of the bulk.[43] It was reported in this reference that the creation of a hole is accompanied by negative system pressure. Similarly, we observe that, as partial drying sets in, the component of the pressure tensor normal to the interface becomes negative.

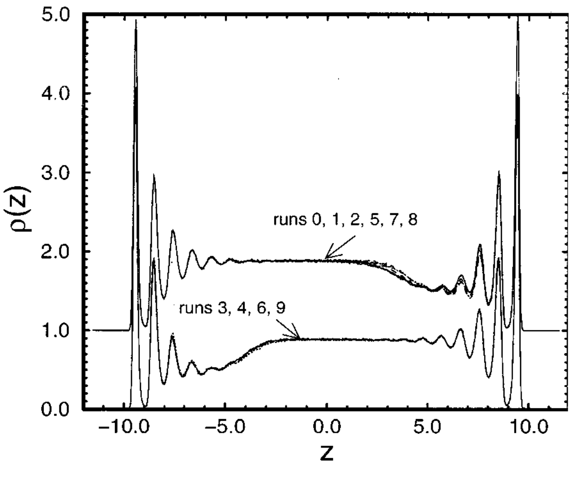

FIG. 10. Density profiles for 10 independent runs at $T=0.8$ for a system size of $L_x=L_y=11.11$ [$\Rightarrow p(z=0)=0.795$ at $T=1$]. As the volume is kept constant, the system separates into two phases as the temperature is lowered to this value: a low density region close to one of the walls and a high density one in the other part of the film. For runs 0, 1, 2, 5, 7, and 8 the density profile is shifted upwards by unity.

V. *T*-DEPENDENCE OF THE SHEAR VISCOSITY

To prevent the phenomenon of partial drying described in the previous section, we change the value of the lateral system size to $L_x=L_y=10.05$. This value results from equilibrium MD simulations of the model confined between perfectly smooth and purely repulsive walls at a normal pressure of $P_{N,\mathrm{ext}}=1$ in the supercooled state, where the system is (almost) incompressible.[30,31] At $T=1$ this leads to $\rho(z=0)=0.99$. It is shown in the upper panel of Fig. 11 that the problem of partial drying is indeed avoided at this density. Furthermore, we observe that the average density at the film center does not change much with temperature. The system thus approaches the limit of an incompressible liquid. Note that, compared to the previous lower density case (see Fig. 4), now the presence of the walls is also "felt" farther inside the film. Furthermore, both the amplitude and the range of the density oscillations grow at lower T.

However, it is also seen from the lower panel of Fig. 11 that, when restricted to $z\in[-5\ 5]$, a quadratic function is a good approximation for the velocity profile. Therefore, we use the coefficient of z^2 obtained from a fit to Eq. (8) to compute the shear viscosity in the film center. The error in shear viscosity, $\Delta\eta_s$, is simply estimated from that of the corresponding fit coefficient. The accuracy of the fit manifests itself in small relative errors in η_s.

From a preliminary study where the shear force is varied, we find that a shear force of $F^e=0.05$ is necessary to obtain a satisfactory signal to noise ratio not only at high, but also at low temperatures (at a temperature of $T=0.35$, for example, a shear force of $F^e=0.01$ leads to a noisy background instead of a parabolic velocity profile). However, it is generally known that, at high shear rates, the response of the system is no longer linear and that the system properties depend on the applied force.[36–40,44–46] Of particular importance for our application is the possibility that the system dynamics may be enhanced compared to the zero-shear case ("shear thinning"). To check if a shear thinning is present at the chosen shear rate, we compare in Fig. 12 the mean square displacement of the chain's center-of-mass in the direction perpendicular to the flow, $g_{3,\perp}$, obtained from a simulation with $F^e=0.05$ with that resulting from a much smaller

Downloaded 27 Sep 2002 to 193.49.39.50. Redistribution subject to AIP license or copyright, see http://ojps.aip.org/jcpo/jcpcr.jsp

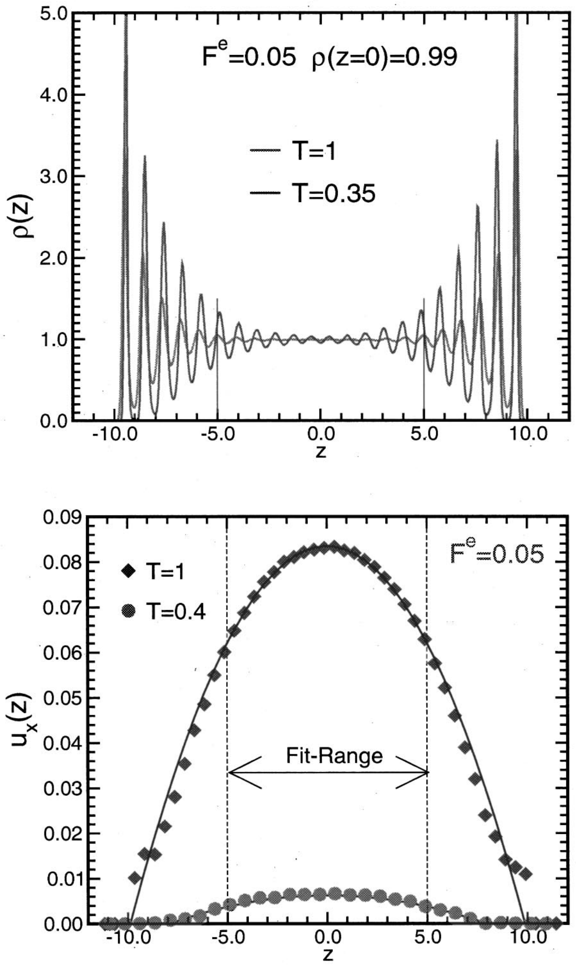

FIG. 11. Upper panel: Density profile of inner particles as obtained from MD-simulations at $T=1$ and $T=0.35$. Contrary to the case of $\rho_0=0.795$, where a relative wide range of a homogeneous inner region is observed (see Fig. 4), now oscillations also occur in the region $z\in[-5\ 5]$ (indicated by vertical solid lines). The magnitude of these density variations is, however, much smaller around $z=0$. Lower panel: Velocity profile for two representative temperatures: $T=1$ (normal liquid state) and $T=0.4$ (supercooled state). Solid lines are results of fits to Eq. (8). The vertical lines mark the fit-range. Note also that, at lower T, the velocity profile already vanishes at an approximate distance of two monomer diameters from the plane of the solid walls ($z=\pm 10$), whereas at higher temperatures $u_x(z)$ vanishes only very close to the solid walls.

choice of $F^e=0.01$. We first note that, at high temperatures, identical results are obtained both for $F^e=0.05$ and for $F^e=0.01$. On the other hand, the (slight) shear force induced acceleration of the dynamics observed at lower temperatures is much weaker than the temperature induced change of the mobility. We will therefore neglect this weak shear thinning, in a study of the temperature dependence of the transport coefficients of the system.

The temperature is varied (along an isochoric line) from $T=1$ (normal liquid state) down to $T=0.3$ (supercooled state). Within this temperature range, the shear viscosity increases by over than two orders of magnitude (from $\eta_s=28.96$ at $T=1$ to $\eta_s=3292.6$ at $T=0.3$). As we will see below, the mode coupling critical temperature of the system is estimated to be $T_c=0.28\pm 0.01$. Thus, the lowest simulated temperature does indeed correspond to the supercooled regime where, in a narrow temperature interval, the shear viscosity increases by an appreciable amount.

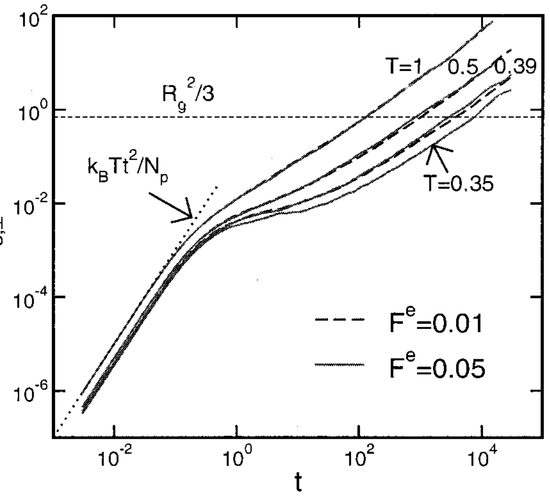

FIG. 12. Log–log plot of the mean square displacement (MSD) of the chain's center-of-mass in the direction perpendicular to the flow, $g_{3,\perp}(t)$, vs time for two values of the applied shear force $F^e=0.05$ (solid lines) and $F^e=0.01$ (long dashed lines). At the high temperature of $T=1$, the data are practically identical for both choices of F^e. At lower temperatures, the higher shear force leads to a slight acceleration of the dynamics. This effect is, however, much weaker than the influence of the temperature on the mobility of the system. The horizontal dashed line indicates the value corresponding to the chain's radius of gyration. The factor 1/3 arises from the fact that three independent spatial coordinates contribute to R_g^2, whereas $g_{3,\perp}(t)$ is obtained using only one independent spatial direction. The diffusion coefficient of the system is obtained from the slope of $g_{3,\perp}(t)\geqslant R_g^2/3$. A solid line indicates the short time behavior of $g_{3,\perp}$ determined by the free (ballistic) motion: $g_{3,\perp}=k_B Tt^2/N_p$ (N_p is the number of monomers per chain). Note that $g_{3,\perp}(t)$ is computed in the film center, i.e., by averaging over monomers with $z(t')\in[-5\ 5]$ for all $t'<t$. In order to illustrate better the gradual formation of a plateau at low temperatures, we also show a curve corresponding to $T=0.35$ for the case of $F^e=0.05$.

We first compare our results on viscosity to that reported in Ref. 47 for a similar polymer model and at practically the same density (of $\rho=1$). In the mentioned reference, the viscosity increases by approximately a factor of 4 when varying the temperature from $T=1$ to $T=0.4$. For the same T-range, we observe a change by approximately a factor of 8.4 [$\eta_s(T=0.4)=244.28$]. The stronger increase of the viscosity with temperature in our model can be ascribed to the presence of the attractive part of the LJ-potential which becomes more important at low temperatures. These forces are absent in Ref. 47 as the LJ-potential is cut off at $r_c=2^{1/6}$, where the potential has its minimum.

Next, we focus on the low temperature bahavior of the system. As the so-called mode coupling theory of the glass transition (MCT) (Refs. 48–50) was rather successful in describing the low temperature dynamics of the present polymer model,[27,29–32] we start an analysis of the shear viscosity in the frame work of the MCT. Due to the idealized version of the MCT, a tagged particle is surrounded by an effective cage built by its neighbors. At high temperatures, the neighboring particles are mobile and the case is flexible so that the tagged particle can leave the cage after a certain time. As the temperature is gradually reduced, the cage becomes more

Downloaded 27 Sep 2002 to 193.49.39.50. Redistribution subject to AIP license or copyright, see http://ojps.aip.org/jcpo/jcpcr.jsp

and more rigid and it takes for the tagged particle longer before it can leave the cage of its neighbors. This behavior is nicely reflected in the time dependence of the mean square displacements, where at low temperatures a plateau is formed for intermediate times indicating this growing period of ''arrest'' (a comparison of the curves for $T=1$, 0.5, 0.39, and 0.35 in Fig. 12, for example, already shows this gradual formation of the plateau). Within this idealized picture, there is a critical temperature T_c at which the cage completely freezes and the tagged particle is arrested for all times. Furthermore, close to T_c, the transport coefficients of the system like the diffusion coefficient and the shear viscosity should obey a power law, provided that $|(T-T_\mathrm{c})/T_\mathrm{c}|\ll 1$. At low temperatures, we thus expect

$$\eta_s(T)=c|T-T_\mathrm{c}|^{-\gamma}. \tag{12}$$

Here, γ is the so-called critical exponent and c is a proportionality constant. Fitting the simulation results on $\eta_s(T)$ to Eq. (12) we have estimated the critical temperature of the system. As Eq. (12) is expected to hold at temperatures close to T_c, the fit was restricted to $T\leqslant 0.5$. This gives $c=8.2\pm 0.5$, $\gamma=1.62\pm 0.1$, and $T_\mathrm{c}=0.28\pm 0.01$. Comparing this result to $T_\mathrm{c}=0.45$, the critical temperature of the same polymer model in the bulk at a (slightly higher) density of $\rho=1.042$,[27] we observe that T_c strongly depends on the system density.

As shown in the upper panel of Fig. 13, Eq. (12) describes well the low temperature part of the simulated data. Furthermore, the deviation from the MCT-law observed for the lowest simulated temperature of $T=0.3$ (which is quite close to $T_\mathrm{c}=0.28$) is not unexpected at all. Such a deviation from the power law has been observed both in experiment[51] and in the (equilibrium) simulations of the same polymer model (for various relaxation times) in the bulk[27,52] and in the film.[31] This is generally related to the fact that the idealized version of the MCT does not take into account thermally activated processes which allow a relaxation of the cage at low temperatures. Using the same simple picture of the ''cage,'' one can say that the tagged particle is not completely arrested in the cage but can leave it after a sufficiently long time.

It is generally known that the transport coefficients of fragile glass formers usually obey the (empirical) Vogel–Fulcher–Tammann (VFT)-law before crossing over to an Arrhenius behavior at much lower temperatures.[53] As shown in the inset of the upper panel of Fig. 13, an Arrhenius-law does not hold in the simulated temperature range. Such a deviation from an Arrhenius behavior is also reported from experiments on aqueous mixtures of Trehalose close to the glass transition.[51] It is therefore interesting to see if the shear viscosity obeys a VFT-formula,

$$\eta_s(T)=\eta_s(\infty)\exp\left(\frac{B}{T-T_0}\right). \tag{13}$$

Here, $\eta_s(\infty)$ is the shear viscosity at infinite temperature, B is a constant, and T_0 is the temperature, where η_s is expected to diverge. Fitting our data to Eq. (13) we obtained $\eta_s(\infty)=13.23\pm 0.13$, $B=0.615\pm 0.036$, and $T_0=0.19\pm 0.005$. As seen from the lower panel of Fig. 14, the quality of the fit is remarkable.

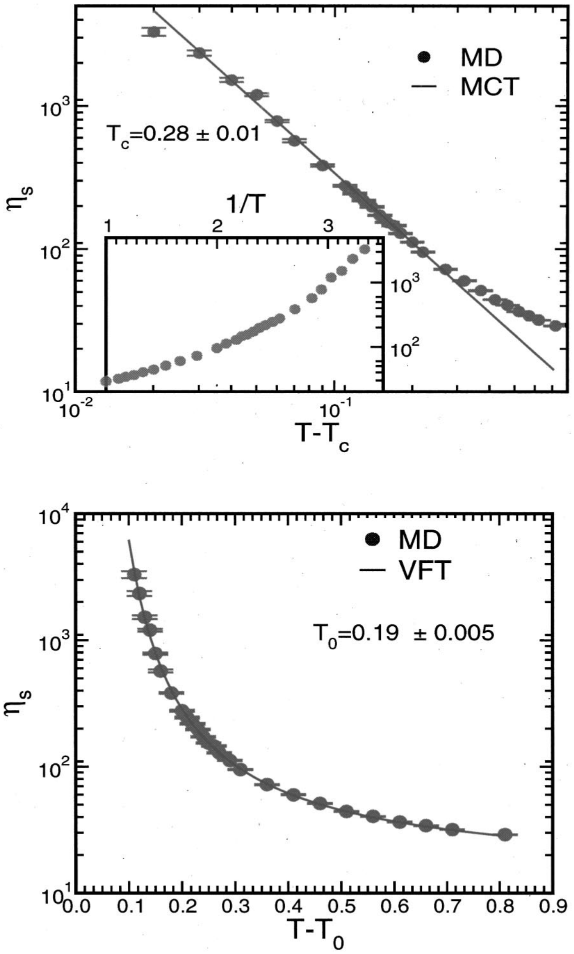

FIG. 13. Upper panel: Log–log plot of the molecular dynamics (MD) results on the shear viscosity vs $T-T_\mathrm{c}$ and the corresponding mode-coupling (MCT) fit [see Eq. (12)]. In applying the MCT fit, only data points with $T\leqslant 0.5$ are taken into account. The inset depicts a linear-log plot of the same data vs $1/T$. Obviously, the data do not follow a straight line. Lower panel: Shear viscosity (symbols) and the corresponding VFT-fit [see Eq. (13)]. As seen here, the data is very well described by the fit at all simulated temperatures.

Next we examine the validity of the Stokes–Einstein relation between the viscosity and the diffusion constant,

$$\frac{k_\mathrm{B}T}{4\pi D_\perp \eta_s}=l=\text{const.} \tag{14}$$

Here, $D_\perp$ is the diffusion coefficient in the direction perpendicular to the flow and l is a length characterizing an elementary diffusive process.[54] The factor 4π corresponds to the assumption that, for the motion of a fluid particle within the same fluid, the slip boundary condition holds (the ''stick'' assumption would lead to a factor of 6π). The diffusion coefficient of the system is obtained from the slope of the mean square displacement of the chain's center-of-mass, $g_{3,\perp}(t)$, at late times, i.e., at times, t, for which $g_{3,\perp}(t)\geqslant R_g^2/3$. As seen from Fig. 12, the motion of the chain's center-of-mass is already diffusive in this limit ($g_{3,\perp}\propto 2D_\perp t$). It must be mentioned here that, as η_s is determined using the data in the film center, we also restrict the computation of $g_{3,\perp}(t)$ to

Downloaded 27 Sep 2002 to 193.49.39.50. Redistribution subject to AIP license or copyright, see http://ojps.aip.org/jcpo/jcpcr.jsp

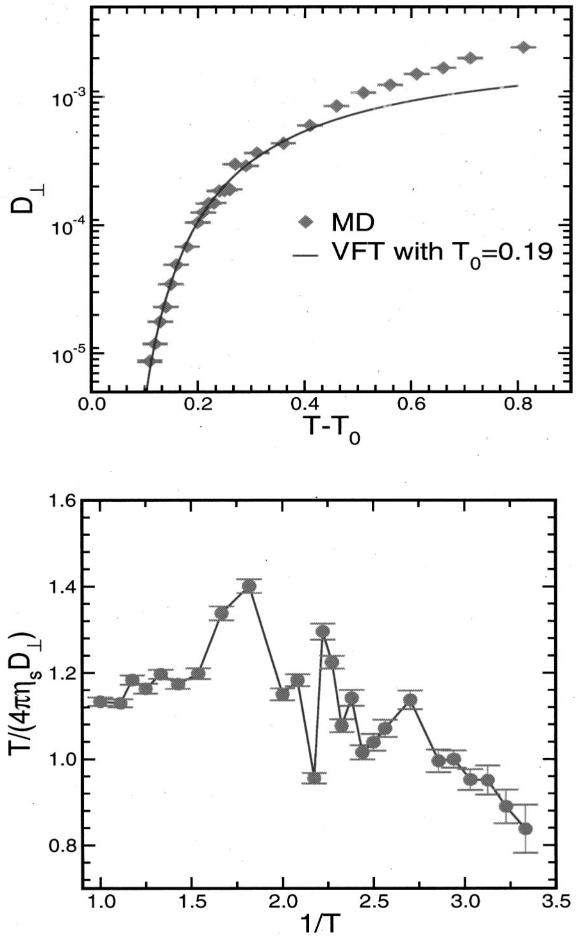

FIG. 14. Upper panel: Linear-log plot of the diffusion constant, $D_\perp$, vs $T-T_0$. $D_\perp$ is obtained from the slope of the mean square displacements of chain's center-of-mass at late times (see Fig. 12). Lower panel: The ratio $l=T/(4\pi D_\perp\eta_s)$ (connected symbols) vs inverse temperature. The irregular changes of l are most likely due to statistical uncertainity in the determination of the diffusion constant.

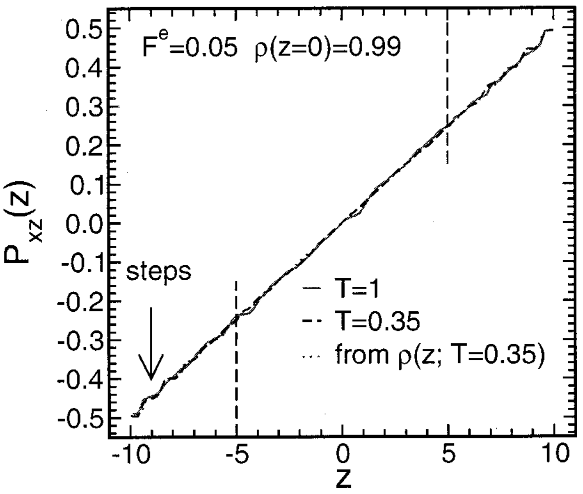

FIG. 15. Off diagonal component of the pressure tensor, $P_{xz}(z)$, as obtained from MD simulations at two representative temperatures $T=1$ (high temperature liquid state) and $T=0.35$ (supercooled state). The thin lines correspond to a direct evaluation of $P_{xz}(z)$ using the Irving–Kirkwood formula [Eq. (17)] whereas the thick (dotted–dashed) line represents the data obtained from $P_{xz}(z)=\int_0^z F^e\rho(z')\mathrm{d}z'$ at $T=0.35$ [Eq. (16)]. Apparently, both methods give identical results. Furthermore, $P_{xz}(z)$ is practically independent of temperature. The slight deviations of the $T=1$ data from the $T=0.35$ one is most probably due to the (by a factor of 10) smaller number of samples. The steps close to the walls reflect the oscillations of density profile (see upper panel of Fig. 11).

this region. $g_{3,\perp}(t)$ is thus computed by averaging only over those monomers which have remained in the region $z\in[-5\ 5]$ for all times $t'<t$.

Results on $D_\perp$ are depicted in the upper panel of Fig. 14. As seen from this panel, $D_\perp$ can be described by a VFT-fit at low temperatures using the same value of $T_0=0.19$ as obtained from fits to the shear viscosity. It is also seen from this figure that, unlike the viscosity which follows a VFT-law for all studied temperatures, only the low temperature part of the diffusion constant exhibits a VFT-behavior. A similar deviation of the diffusion coefficient from a VFT-law at high temperatures has also been observed in the equilibrium studies of the present model in the bulk.[43] The knowledge of $D_\perp(T)$ and $\eta_s(T)$ can now be used for a check of Eq. (14). The lower panel of Fig. 14 shows $l\equiv k_\mathrm{B}T/(4\pi D_\perp\eta_s)$ versus inverse temperature. First, we note that the resulting value of $l\approx 1.2$ is quite reasonable as it indicates that an elementary diffusive process approximately corresponds to an average displacement of a monomer diameter. Furthermore, l is rather constant with respect to a variation of temperature. However, a systematic decrease seems to set in for lower T. In fact, a decrease of l with $1/T$ has been observed in MD simulations of SiO_2 (Ref. 55) and in experiments on fragile glass formers *below* the critical temperature of the corresponding system.[56–62]

VI. LOCAL VISCOSITY

For a fluid moving between flat parallel walls the knowledge of the off-diagonal component of the pressure tensor, $P_{xz}(z)$, on the one hand and that of the velocity profile, $u_x(z)$, on the other hand allows the calculation of the *local* viscosity,[11,20,63]

$$\eta(z)=-\lim_{F^e\to 0}\frac{P_{xz}(z)}{u_x'(z)}. \tag{15}$$

Figure 15 depicts $P_{xz}(z)$ for two representative temperatures of $T=1$ (high temperature liquid state) and $T=0.35$ (supercooled state). As seen from this figure, $P_{xy}(z)$ is rather insensitive to a change of T. This is directly related to the fact that also the density profiles hardly change with temperature (see the upper panel of Fig. 11). In fact, for a fluid flow between planar walls, it follows from the momentum conservation equation that $\partial P_{xz}(z)/\partial z=F^e\rho(z)$ (see, for example, Ref. 20). Taking into account that shear stress $(=-P_{xz})$ vanishes in the film center $(z=0)$, a simple integration then gives

$$P_{xz}(z)=\int_0^z F^e\rho(z')\mathrm{d}z'. \tag{16}$$

However, a more general expression for computing $P_{xz}(z)$ in a planar system is the Irving–Kirkwood formula for the pressure tensor,[20,41,64]

Downloaded 27 Sep 2002 to 193.49.39.50. Redistribution subject to AIP license or copyright, see http://ojps.aip.org/jcpo/jcpcr.jsp

$$\mathbf{P}(z)=\rho(z)k_{\mathrm{B}}T\hat{\mathbf{1}} -\frac{1}{2A}\left\langle \sum_{i\neq j}^{N} \frac{\boldsymbol{r}_{ij}\boldsymbol{r}_{ij}}{r_{ij}} U'(r_{ij}) \frac{1}{|z_{ij}|}\Theta\left(\frac{z-z_i}{z_{ij}}\right)\Theta\left(\frac{z_j-z}{z_{ij}}\right)\right\rangle . \tag{17}$$

In Eq. (17) $\Theta(x)$ denotes the Heaviside step function $[\Theta(x)=0$ if $x<0$ and 1 for $x>0]$, U is the pair potential, and U' its derivative with respect to interparticle distance, $\boldsymbol{r}_{ij}=\boldsymbol{r}_j-\boldsymbol{r}_i(r_{ij}=|\boldsymbol{r}_{ij}|)$ and $\hat{\mathbf{1}}$ stands for the 3×3 unit matrix.

Figure 15 compares $P_{xz}(z)$ obtained by an evaluation of the Irving–Kirkwood formula with that of Eq. (16). Obviously, both approachs give identical results. However, as the velocity profile depends on temperature, a variation of the local viscosity profile with T is be expected.

To apply Eq. (15) for a computation of the local viscosity, the velocity gradient must first be determined. For this purpose, we have used two different approaches. First, the velocity profile is fitted to a sixth order symmetric polynomial,

$$u_x(z)=u_0+Az^2+Bz^4+Cz^6. \tag{18}$$

The resulting coefficients A, B, and C are then used to compute

$$\partial u_x(z)/\partial z=2Az+4Bz^3+6Cz^5. \tag{19}$$

Note that the coefficients resulting from a fit to Eq. (18) do in general depend on the fit range. However, it is clear that we are interested in taking into account the largest possible data set extending towards the region where the velocity profile (almost) vanishes. As the effective position of the walls (where the velocity profile vanishes) is not precisely known, we examine two possible choices to see if the results on the velocity gradient depend on the particular fit range.

As an alternative, we have also determined $u_x'(z)$ by computing the slope of the line which best fits a small number of data points around the desired point, say z. Varying the number of neighboring points taken into account in the linear regression procedure, we find that a set of 5 points (the data point z and two points on each side of it) yields satisfactory results on $u_x'(z)$. Figure 16 depicts results on the velocity gradient, $u_x'(z)$, for two temperatures of $T=1$ (upper panel) and $T=0.41$ (lower panel). It is seen from this figure that $u_x'(z)$ does not depend much on the applied method. However, larger numerical uncertainty is observed, when the velocity gradient is computed applying the local linear regression method. This can have large impact of $\eta(z)$ for $u_x'(z)$ is a small quantity and appears in the denominator of Eq. (15). To avoid this problem, we use $u_x'(z)$ computed via Eqs. (18) and (19).

A further source of error in computing $\eta(z)$ is the fact that not only $\partial u_x(z)/\partial z$ but also $P_{xz}(z)$ vanishes at the film center. As a consequence, a small statistical error in P_{xz} is directly amplified by a (huge) factor of $1/u_x'(z)$ thus leading to large errors in $\eta(z)$. This problem is fully avoided when the use of Eq. (19) [which guarantees that $u_x'(z)\propto z$ when $z\to 0$] is combined with a linear approximation to $P_{xz}(z)$ in the film center, i.e., when $P_{xz}=F^e\rho_0 z$ for $z\in[-5\ 5]$, say. The validity of such an approximation is easily seen from Fig. 15. Note that the linear approximation for P_{xz} is *not* applied outside the region $z\in[-5\ 5]$ but we use simulation results on this quantity.

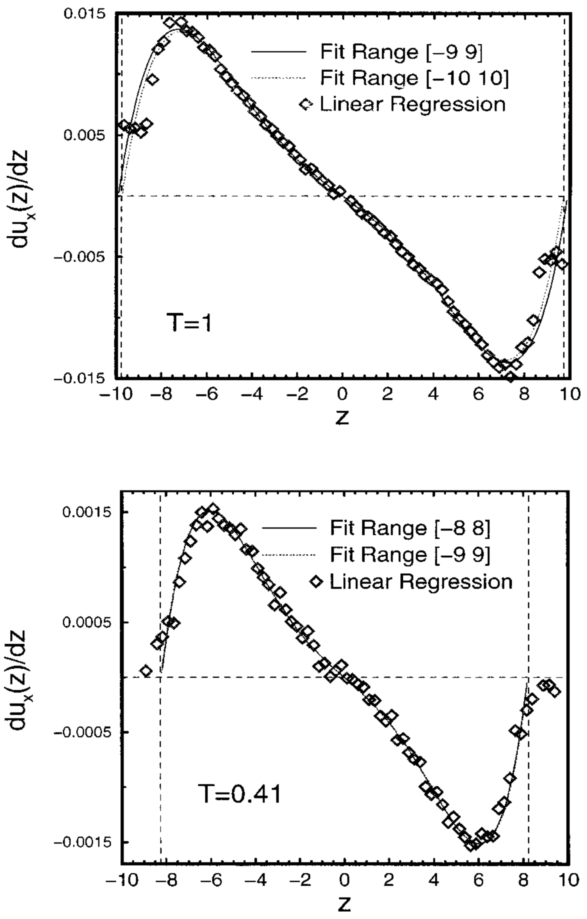

FIG. 16. Upper panel: Velocity gradient, $u_x'(z)=\partial u_x(z)/\partial z$, at $T=1$ (high temperature liquid state). Lines correspond to the result obtained by first fitting the velocity profile to a sixth order symmetric polynomial, $u_x(z)=u_0+Az^2+Bz^4+Cz^6$, and then using the coefficients A, B, and C to compute $\partial u_x(z)/\partial z=2Az+4Bz^3+6Cz^5$. In applying the polynomial fit to $u_x(z)$, the fit range is varied. As seen from this panel, the result on $u_x'(z)$ does not depend much on the fit range. Furthermore, the velocity gradient is also obtained in a different way (squares): For a given data point, z, $u_x'(z)$ is computed as the slope of a line which best fits to $u_x(z)$. Here, 5 data points centering at z are taken into account for the linear regression. Similar results are also obtained for 7 points. The vertical dashed lines indicate the effective position of the wall, where the velocity gradient vanishes and thus the local viscosity, $\eta(z)=-P_{xz}(z)/u_x'(z)$, is expected to diverge: $z_{\mathrm{wall}}(T=1)=9.75$ (see also Fig. 17). Lower panel: Same as in the upper panel, but for a lower temperature of $T=0.41$ (supercooled state). Now, $z_{\mathrm{wall}}(T=0.41)=8.25$.

Figure 17 shows results on the reduced local viscosity $\eta(z)/\eta_s$ for two characteristic temperatures of $T=1$ (normal liquid state, upper panel) and $T=0.41$ (supercooled state, lower panel). Each panel contains two curves corresponding to different choices of the range used to fit the data to Eq. (18). Obviously, the result on $\eta(z)$ does not depend much on the chosen fit range. In particular, for a wide region around the film center, no dependence on the applied fit range is seen. However, a slight variation of the result with the fit range is observed for $T=1$. We will take the average of these both curves for further investigation.

The increase of the viscosity close to the walls can be

Downloaded 27 Sep 2002 to 193.49.39.50. Redistribution subject to AIP license or copyright, see http://ojps.aip.org/jcpo/jcpcr.jsp

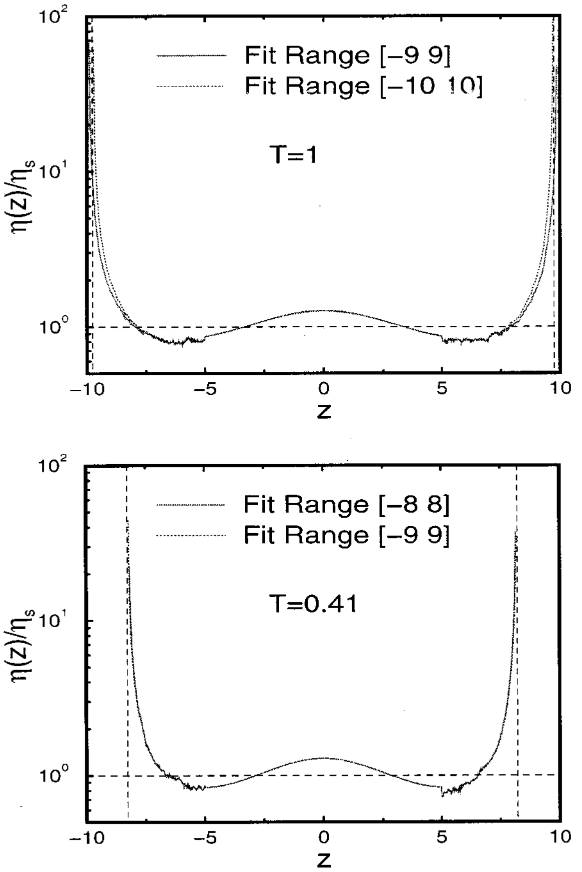

FIG. 17. Upper panel: Reduced local viscosity, $\eta(z)/\eta_s$, computed using Eq. (15) at $T=1$ (high temperature liquid state). Different lines correspond to different fit ranges used for a computation of the velocity gradient [which serves as input for $\eta(z)=-P_{xz}/u'_x(z)$] via fits to Eq. (18). In the film center, i.e., for $z\in[-5\ 5]$, the off-diagonal component of the pressure tensor has been approximated by $P_{xz}(z)=F^e\rho_0 z$. A look at Fig. 15 shows that this approximation is practically exact. The vertical lines mark the effective position of the walls, estimated from $u'_x(z)=0$ (see Fig. 16). The horizontal dashed line marks $\eta(z)/\eta_s=1$. Note that $u'_x(z)$ is a smooth function for all z. The only source of statistical noise is thus P_{xz}. As this quantity is approximated by a straight line for $z\in[-5\ 5]$, the statistical noise can only occur beyond this region. Lower panel: Same as in the upper panel but for $T=0.41$.

rationalized as follows: Close to the wall, the particles are much stronger attracted and are at least partially trapped in the wall potential. Obviously, a stronger lateral force must be applied in order to "shear" a fluid layer in contact with such a "trapped" layer compared to the case where both layers are mobile. In other words, the proportionality constant between the stress tensor and the velocity gradient increases when the wall is approached [see Eq. (15)].

The observed increase of the local viscosity in the vicinity of the wall has also been reported from the MD simulations of oligomer fluids.[45] Note, however, that in the mentioned reference, only two distinct layers are investigated: a central layer and a layer close to the wall, whereas we consider the whole spatial dependence of the shear viscosity. Our approach is in fact identical to that in Ref. 20. There, an increase in shear viscosity close to a solid wall is reported for a system with WCA interaction at an average density of $\bar{\rho}=0.8362$ and average temperature of $\bar{T}=0.97$.[67]

As to the variation of $\eta(z)$ at the film center, similar behavior also is observed in MD simulations of a WCA system.[65] Note that Eq. (15) represents a local approximation to a more general formula which also takes into account nonlocal effects, $P_{xz}(z)=\int \eta(z;z-z')dz'/u'(z')$.[11,65] Therefore, the (rather unexpected) variations of $\eta(z)$ at the film center are probably related to a violation of this local approximation.[65]

Recall that η_s is computed from fits to Eq. (8) within the range $z\in[-5\ 5]$. It is therefore interesting to see if some agreement can be found between η_s and the average of $\eta(z)$ over the same interval. For $T=1$ we obtain $\int_{-5}^{5}\eta(z,T=1)dz/10=31.36$ which lies about 8% above the value of $\eta_s(T=1)=28.96$. The agreement is slightly better at the lower temperature of $T=0.41$, where $\int_{-5}^{5}\eta(z,T=0.41)dz/10=230.1$ thus being only 5% above the value of $\eta_s(T=0.41)=218.33$. Thus, using the above approach, we are able to determine $\eta(z)$ within a relative accuracy of 10%.

Note that, compared to $T=1$, at $T=0.41$ the region where $\eta(z)$ starts to rise is shifted towards the film center by approximately 1.5 monomer diameter. Motivated by this observation, we define an effective position of the wall, z_{wall}, as the plane where $\eta(z)$ diverges. This is in fact identical to the plane (close to the wall) where the velocity gradient vanishes (see Fig. 16). Using this criterion, we obtain from Fig. 16, $z_{\mathrm{wall}}\approx 9.75$ for $T=1$ and $z_{\mathrm{wall}}\approx 8.25$ for $T=0.41$.

Thus, the effective position of the wall moves towards the film center as T is lowered. Note that the fluid–wall attraction becomes more important at lower temperatures. Therefore, our result is consistent with the experimental observation that the hydrodynamic thickness of the system decreases when the fluid–wall attraction is increased.[66]

Note also that, in the whole z-range between the film center and the walls, $\eta(z)/\eta_s$ varies approximately within the same range for both depicted temperatures. Recalling that the sharp rise in $\eta(z)$ sets in at different z-values, it is therefore interesting to look at the behavior of $\eta(z)/\eta_s$ not as a function of the distance from the film center, but versus the distance from an effective wall placed at $z_{\mathrm{wall}}(T)$. For this purpose we first symmetrize the curves for $\eta(z)/\eta_s$ and then plot them versus $z-z_{\mathrm{wall}}(T)$.

Figure 18 shows $\eta(z,T)/\eta_s(T)$ versus $z-z_{\mathrm{wall}}(T)$ for $T=1$ and $T=0.41$. As seen from this figure, despite the strong variation of the shear viscosity with temperature [compare $\eta_s(T=0.41)=218.33$ to $\eta_s(T=1)=28.96$], the reduced and shifted curves approximately superimpose for both temperatures. The temperature dependence of the local viscosity thus seems to separate from its spatial dependence, if the spatial variable is defined with respect to a slightly temperature dependent reference frame, $z_{\mathrm{wall}}(T)$.

VII. CONCLUSION

Results of nonequilibrium molecular dynamics simulations on a nonentangled sheared polymer melt confined between walls are presented. The outer layers of the solid walls have been modeled as a triangular lattice with harmonic springs. For the interaction between the wall and the fluid

Downloaded 27 Sep 2002 to 193.49.39.50. Redistribution subject to AIP license or copyright, see http://ojps.aip.org/jcpo/jcpcr.jsp

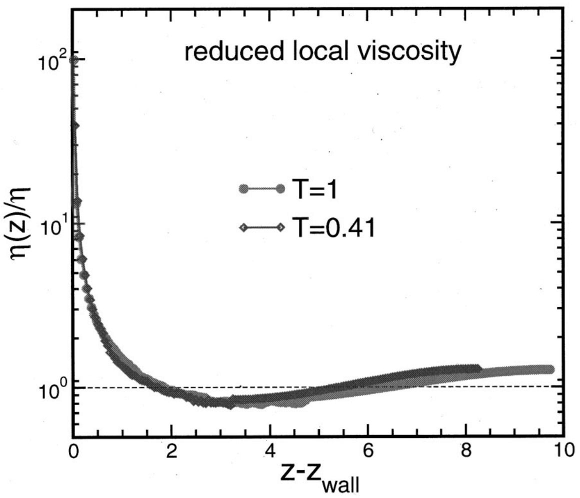

FIG. 18. Local viscosity, $\eta(z,T)$, in units of the shear viscosity, $\eta_s(T)$, for $T=1$ (circles) and $T=0.41$ (diamonds) vs the distance from the effective position of the wall, i.e., vs $z-z_{\text{wall}}(T)$. Note that the shear viscosities at these two temperatures differ by approximately one order of magnitude $[\eta_s(T=1)=28.96$ compared to $\eta_s(T=0.41)=218.33]$. Despite this strong variation with temperature, the reduced local viscosities superimpose.

atoms (monomers) a Lennard-Jones potential is used. We study the influence of the parameters of the interaction between wall atoms and monomers on the boundary conditions. A large slip is observed when the wall and fluid atoms are "indistinguishable," i.e., if $\epsilon_{ij}=1$ and $\sigma_{ij}=1$ for $[ij \in \{\text{mm}, \text{wm}, \text{ww}\}]$, whereas the choice of $\epsilon_{\text{wm}}=2\epsilon_{\text{mm}}$ along with $\sigma_{\text{wm}}=0.89\sigma_{\text{mm}}$ leads to a stick boundary condition. It is also shown that this observation is consistent with theoretical predictions.[22,23]

It is also observed that a temperature profile forms when the inner part of the system is not directly thermostated but is only allowed to exchange energy with (thermostated) walls. These temperature profiles are well described by hydrodynamics[26] thus allowing an estimation of the heat conductivity of the system. We find that the heat conductivity of the present polymer model varies only slowly with temperature, in qualitative agreement with experimental results.[42]

Furthermore, we study the temperature dependence of the shear viscosity in a T-interval ranging from the normal liquid state to the supercooled region. We are aware of the fact that, due to a certain inhomogeneity in the film, the overall shear viscosity is not necessarily identical to that of the corresponding bulk system. Therefore, we restrict the data analysis in computing $\eta_s(T)$ to a region around the film center where bulklike properties are expected. We also address the question of whether or not a shear thinning is present at the chosen value of the shear force ($F^e=0.05$). The strict answer to this question being positive, we show that the effect is quite small and fully dominated by the dependence of the transport properties on temperature.

An enhanced increase of η_s at lower temperatures is observed. It is found that this increase can not be described by an Arrhenius law but it can be well fitted both to a power law (like that predicted by the mode-coupling theory) and to a Vogel–Fulcher–Tammann law. The mode-coupling critical temperature of the system at a density of $\rho=0.99$ is thus determined to be $T_c=0.28\pm0.01$, whereas the VFT-temperature is found to be $T_0=0.19\pm0.005$. For the lowest simulated temperatures, which are quite close to T_c, we observe deviations from the MCT-power law. These deviations are expected for the idealized version of the MCT does not take into account the thermally activated processes, which become dominant at low temperatures. Again, similar observations are made on the experimental side.[51]

We also determine the diffusion coefficient, $D_\perp$, using the mean square displacements of the chain's center-of-mass in direction perpendicular to the flow. It is then shown that the quantity $T/(D_\perp \eta_s)$ is practically constant at high temperatures (Stokes–Einstein relation), whereas the beginning of a temperature dependence is observed at low T. The corresponding length scale $l=T/(4\pi D_\perp \eta_s)$ is found to be of order of a monomer size, which is quite reasonable as l is associated with an elementary diffusive process.

An analysis of the local viscosity is the subject of the last part of this report. An increase of the local viscosity is observed when approaching the walls. In addition to that, using the sharp rise of $\eta(z)$, we estimate z_{wall}, the effective position of the wall. We find that, as temperature decreases, z_{wall} moves towards the inner part of the film thus leading to a decrease of the effective (or hydrodynamic) width of the system. The significance of $z_{\text{wall}}(T)$ is demonstrated showing that the (symmetrized) curves of $\eta(z)/\eta_s$ at various temperatures superimpose if they are compared with respect to the corresponding wall position, i.e., if the data are plotted vs $z-z_{\text{wall}}(T)$. This implies that the spatial and temperature dependencies of the local viscosity separate if, instead of $z=0$, the (temperature dependent) reference plane $z_{\text{wall}}(T)$ is used.

ACKNOWLEDGMENTS

We would like to express our thanks to J. Baschnagel, J. Horbach, M. Fuchs, and M. Müser for useful discussions. We gratefully acknowledge the financial support of the "Deutsche Forschungsgemeinschaft" (DFG) under the Project No. SFB262 and by BMBF under the Project No. 03N6015 and by the project "Multifunktionale Werkstoffe und Miniaturisierte Funktionseinheiten." We are also indebted to the European Science Foundation for financial support by the ESF Program on "Experimental and Theoretical Investigations of Complex Polymer Structures" (SUPERNET). Generous grants of simulation time by the computer center at the University of Mainz (ZDV), the NIC in Jülich, and the RHRK in Kaiserslautern are also acknowledged.

[1] R. Kohlrausch, Pogg. Ann. Phys. **12**, 393 (1847); G. Adam and J. H. Gibbs, J. Chem. Phys. **43**, 139 (1965); R. Zallen, *The Physics of Amorphous Solids* (Wiley, New York, 1983).

[2] J. Jäckle, Rep. Prog. Phys. **49**, 171 (1986); W. Götze and L. Sjögren, *ibid.* **55**, 241 (1992).

[3] M. H. Cohen and D. Turnbull, J. Chem. Phys. **31**, 1164 (1959); **34**, 120 (1961); **52**, 3038 (1970); M. H. Cohen and G. S. Grest, Phys. Rev. B **20**, 1077 (1979).

[4] K. L. Ngai, R. W. Rendell, A. K. Rajagopal, and S. Teitler, Ann. N.Y. Acad. Sci. **484**, 150 (1986); K. L. Nagi and G. B. Wright, J. Non-Cryst. Solids **131-133** (1991); **172-174** (1994); **235-237** (1998).

[5] R. Schilling, in *Disorder Effects on Relaxational Processes,* edited by R.

Downloaded 27 Sep 2002 to 193.49.39.50. Redistribution subject to AIP license or copyright, see http://ojps.aip.org/jcpo/jcpcr.jsp

Richert and A. Blumen (Springer, Berlin, 1994); R. Richert, J. Phys. Chem. B **101**, 6323 (1997); M. D. Ediger, Annu. Rev. Phys. Chem. **51**, 99 (2000).

[6] S. R. Nagel, G. S. Grest, S. Feng, and L. M. Schwartz, Phys. Rev. B **34**, 8667 (1986); R. M. Ernst, S. R. Nagel, and G. S. Grest, *ibid.* **43**, 8070 (1991).

[7] W. Kob, J. Phys.: Condens. Matter **11**, R85 (1999); J. Horbach and W. Kob, Phys. Rev. B **60**, 3169 (1999); W. Kob, in *Annual Review of Computational Physics*, edited by D. Stauffer (World Scientific, Singapore, 1995); K. Binder and W. Kob, in *Analysis of the Composition and Structure of Glass and Glass Ceramics*, edited by H. Bach and D. Krause (Springer, Berlin, 1999), pp. 255–267; W. Kob and K. Binder, *ibid.*, pp. 344–356; W. Paul and J. Baschnagel, in *Monte Carlo and Molecular Dynamics Simulation in Polymer Science*, edited by K. Binder (Oxford University Press, New York, 1995); K. Binder, J. Baschnagel and W. Paul, Prog. Polym. Sci. (in press).

[8] P. Espagñol and I. Zúñiga, J. Chem. Phys. **98**, 574 (1993).

[9] L. Bocquet and J.-L. Barrat, Phys. Rev. E **49**, 3079 (1993).

[10] D. J. Evans and J. P. Morriss, Comput. Phys. Rep. **1**, 297 (1984).

[11] D. J. Evans and G. P. Morriss, *Statistical Mechanics of Nonequilibrium Liquids* (Academic, London, 1990).

[12] J.-P. Hansen and I. R. McDonald, *Theory of Simple Liquids* (Academic, London, 1990).

[13] M. Pütz, K. Kremer, and G. S. Grest, Europhys. Lett. **49**, 735 (2000).

[14] V. P. Sokhan, D. Nicholson, and N. Quirke, J. Chem. Phys. **115**, 3878 (2001).

[15] M. Kröger and S. Hess, Phys. Rev. Lett. **85**, 1128 (2000).

[16] K. Kremer, G. S. Grest, and I. Carmesin, Phys. Rev. Lett. **61**, 566 (1988).

[17] K. Kremer and G. S. Grest, J. Chem. Phys. **92**, 5057 (1990).

[18] P. E. Rouse, J. Chem. Phys. **21**, 1272 (1953).

[19] P. G. de Gennes, *Scaling Concepts in Polymer Physics* (Cornell University Press, Ithaca, 1979).

[20] B. D. Todd, D. J. Evans, and P. J. Daivis, Phys. Rev. E **52**, 1627 (1995).

[21] D. J. Evans, Phys. Rev. A **23**, 2622 (1981).

[22] J.-L. Barrat and L. Bocquet, Phys. Rev. Lett. **82**, 4671 (1999).

[23] J.-L. Barrat and L. Bocquet, Faraday Discuss. **112**, 119 (1999).

[24] P. A. Thompson and M. O. Robbins, Phys. Rev. A **41**, 6830 (1990).

[25] A. Jabbarzadch, J. D. Atkinson, and R. I. Tanner, J. Chem. Phys. **110**, 2612 (1999).

[26] B. D. Todd and D. J. Evans, Phys. Rev. E **55**, 2800 (1997).

[27] C. Bennemann, W. Paul, K. Binder, and B. Dünweg, Phys. Rev. E **57**, 843 (1998).

[28] H. Meyer and F. Müller-Plate, J. Chem. Phys. (to be published).

[29] C. Bennemann, J. Baschnagel, and W. Paul, Eur. Phys. J. B **10**, 323 (1999).

[30] F. Varnik, J. Baschnagel, and K. Binder, J. Phys. IV **10**, 239 (2000).

[31] F. Varnik, J. Baschnagel, and K. Binder, Phys. Rev. E **65**, 021507 (2002).

[32] F. Varnik, J. Baschnagel, and K. Binder, Eur. Phys. J. E, special issue on properties of thin polymer films (in press).

[33] D. Y. C. Chan and R. G. Horn, J. Chem. Phys. **83**, 5311 (1985).

[34] J. N. Israelachvili, J. Colloid Interface Sci. **110**, 263 (1986).

[35] E. T. Watts, J. Krim, and A. Widom, Phys. Rev. B **41**, 3466 (1990).

[36] J. Koplik and J. R. Banavar, Phys. Rev. Lett. **80**, 5125 (1998).

[37] G. S. Grest, Phys. Rev. Lett. **76**, 4979 (1996).

[38] R. Khare, J. J. de Pablo, and A. Yethiraj, Macromolecules **29**, 79101 (1996).

[39] E. Manias, G. Hadziioannou, and G. ten Brinke, Langmuir **12**, 4587 (1996).

[40] S. Barsky and M. O. Robbins, Phys. Rev. E **63**, 021801 (2001).

[41] J. H. Irving and J. G. Kirkwood, J. Chem. Phys. **18**, 817 (1950).

[42] P. K. Dixon and S. R. Nagel, Phys. Rev. Lett. **61**, 341 (1988).

[43] C. Bennemann, Ph.D. thesis, Universität Mainz, 1998.

[44] W. Xue and G. S. Grest, Phys. Rev. Lett. **64**, 419 (1990).

[45] E. Manias, I. Bitsanis, G. Hadziioannou, and G. ten Brinke, Europhys. Lett. **33**, 371 (1996).

[46] S. Barsky and M. O. Robbins, Phys. Rev. E **65**, 021808 (2002).

[47] R. Yamamoto and A. Onuki, J. Phys.: Condens. Matter **12**, 6323 (2000).

[48] W. Götze, in *Les Houches 1989, Session LI*, edited by J. P. Hansen, D. Levesque, and J. Zinn-Justin (North–Holland, Amsterdam, 1989), pp. 287–503.

[49] W. Götze and L. Sjögren, Transp. Theory Stat. Phys. **24**, 801 (1995).

[50] W. Götze and L. Sjögren, Rep. Prog. Phys. **55**, 241 (1992).

[51] D. P. Miller, J. J. de Pablo, and H. R. Corti, J. Phys. Chem. B **103**, 10243 (1999).

[52] C. Bennemann, W. Paul, J. Baschnagel, and K. Binder, J. Phys.: Condens. Matter **11**, 2179 (1999).

[53] J. Wong and C. A. Angell, *Glass: Structure by Spectroscopy* (Marcel Dekker, Basel, 1976).

[54] S. Glasstone, K. J. Laidler, and H. Eyring, *The Theory of Rate Processes* (McGraw–Hill, New York, 1941).

[55] J. Horbach and W. Kob, Phys. Rev. B **60**, 3169 (1999).

[56] F. Fujara, B. Geil, H. Silescu, and G. Fleischer, Z. Phys. B: Condens. Matter **88**, 195 (1992).

[57] I. Chang, F. Fujara, B. Geil, G. Heuberger, T. Mangel, and H. Silescu, J. Non-Cryst. Solids **172-174**, 248 (1994).

[58] M. T. Cicerone, F. R. Blackburn, and M. D. Ediger, Macromolecules **28**, 8224 (1995).

[59] M. T. Cicerone and M. D. Ediger, J. Chem. Phys. **104**, 7210 (1996).

[60] M. D. Ediger, C. A. Angell, and S. R. Nagel, J. Phys. Chem. **100**, 13200 (1996).

[61] F. H. Stillinger and J. A. Hodgdon, Phys. Rev. E **50**, 2064 (1994).

[62] N. Menon and S. R. Nagel, Phys. Rev. Lett. **73**, 963 (1994).

[63] L. D. Landau and E. M. Lifschitz, *Hydrodynamik* (Akademie Verlag, Berlin, 1991), Vol. VI.

[64] F. Varnik, J. Baschnagel, and K. Binder, J. Chem. Phys. **113**, 4444 (2000).

[65] E. Akhmatskaya, B. D. Todd, P. J. Daivis, D. J. Evans, K. E. Gubbins, and L. A. Pozhar, J. Chem. Phys. **106**, 4684 (1997).

[66] J.-M. Georges, S. Millot, J.-L. Loubet, and A. Tonck, J. Chem. Phys. **98**, 7345 (1993).

[67] In this reference, the system was thermostated by heat transfer to the walls only. As shown in Sec. IV, this usually leads to a higher temperature in the fluid than imposed to the walls. Furthermore, a temperature profile forms across the pore whence the meaning of T as the average temperature over the whole fluid.

Downloaded 27 Sep 2002 to 193.49.39.50. Redistribution subject to AIP license or copyright, see http://ojps.aip.org/jcpo/jcpcr.jsp